THE RADIOMETRIC CALIBRATION AND THE SENSOR ARRANGEMENT VERIFICATION OF ONGLAISAT KT90 TELESCOPE PRIOR TO LAUNCH

Chien-Ying Yang[1]*, Chen-Yu Chan[2], Po-Hsuan Huang[3], Shih-Fang Liao[4], Tse Li[5], Jie-Rou Shang[6], Yu-Lin Tsai[7], Akihiro Ishikawa[8], Nakasuka Shinichi[9]

[1]Assistant Researcher, Taiwan Space Agency (TASA), Taiwan
8F, 9 Prosperity 1st Road, Hsinchu Science Park, HsinChu City 300, Taiwan
Email: cyyang@tasa.org.tw

[2]Associate Researcher, Taiwan Space Agency (TASA), Taiwan
8F, 9 Prosperity 1st Road, Hsinchu Science Park, HsinChu City 300, Taiwan
Email: cychan@tasa.org.tw

[3]Engineer, Taiwan Space Agency (TASA), Taiwan
8F, 9 Prosperity 1st Road, Hsinchu Science Park, HsinChu City 300, Taiwan
Email: pohsuan@tasa.org.tw

[4]Assistant Researcher, Taiwan Space Agency (TASA), Taiwan
8F, 9 Prosperity 1st Road, Hsinchu Science Park, HsinChu City 300, Taiwan
Email: maggie.liao@tasa.org.tw

[5]Assistant Engineer, Taiwan Space Agency (TASA), Taiwan
8F, 9 Prosperity 1st Road, Hsinchu Science Park, HsinChu City 300, Taiwan
Email: leetse@tasa.org.tw

[6]Assistant Researcher, Taiwan Space Agency (TASA), Taiwan
8F, 9 Prosperity 1st Road, Hsinchu Science Park, HsinChu City 300, Taiwan
Email: bandyshang@tasa.org.tw

[7]Associate Researcher, Taiwan Space Agency (TASA), Taiwan
8F, 9 Prosperity 1st Road, Hsinchu Science Park, HsinChu City 300, Taiwan
Email: morphling@tasa.org.tw

[8]Project Academic Specialist, The University of Tokyo, Japan
7-3-1 Hongo, Bunkyo-ku, Tokyo 113-8656 Japan
Email: ishikawa@space.t.u-tokyo.ac.jp

[9]Professor, The University of Tokyo, Japan
7-3-1 Hongo, Bunkyo-ku, Tokyo 113-8656 Japan
Email: nakasuka@space.t.u-tokyo.ac.jp

KEY WORDS: Remote sensing instrument, CubeSat, Radiometric calibration, Sensor arrangement

ABSTRACT: The ONboard Globe-Looking And Imaging SATellite (ONGLAISAT) project is expected to launch a 6U Remote Sensing CubeSat with Ultra High Resolution from the International Space Station in 2024. This project is a collaboration between the Intelligent Space Systems Laboratory (ISSL) in the Department of Aeronautics and Astronautics at the University of Tokyo, ArkEdge Space Co., Ltd., Space BD, Inc., and the Taiwan Space Agency (TASA). In this project, TASA is responsible for developing the major remote sensing instrument (RSI) payload, which consists of a Korsch-type telescope design and a time delay integral (TDI) CMOS sensor.

In this article, we present the radiometric calibration method and arrangement verification method of the sensor on the ONGLAISAT. The sensor's response with respect to irradiance can be measured using uniform irradiance. Additionally, the distances between two line sensor chips are verified by measuring the RSI rotation angles against a double-slit target.

1. INTRODUCTION

In recent years, nanosatellites have gained prominence due to their ability to achieve goals at a lower cost and within shorter development cycles. The ONboard Globe-Looking And Imaging SATellite (ONGLAISAT) project (Chan et al. 2022.) is one of the CubeSat projects by the Taiwan Space Agency (TASA) aimed at developing a 6U Ultra High-Resolution Remote Sensing CubeSat. This project was developed through a collaboration between TASA, the Intelligent Space Systems Laboratory (ISSL) at the University of Tokyo's Department of Aeronautics and Astronautics, ArkEdge Space Co., Ltd., and Space BD, Inc. ONGLAISAT is scheduled for launch from the International Space Station in 2024.

Figure 1. The 6U CubeSat ONLAISAT.

Figure 1 shows the overview structure of ONGLAISAT. The Remote Sensing Instrument (RSI) payload consists of a Korsch-type telescope design and a time delay integral (TDI) CMOS line sensor. The sensor has the capability to detect light within the wavelength range of 450-900 nm. Figure 2 shows that eight chips in this sensor, each chip with a pixel size 0.005 mm and 1024 pixels, including 16 dummy pixels, are organized into two rows and produce a 5772-pixel-wide image. In the ONGLAISAT project, the TDI stage is planned to use 1 TDI stage and 8 TDI stages. In this article, we propose the radiometric calibration method for ONGLAISAT and measure the distance between sensors in different rows.

Figure 2. The sensor arrangements. Chip number is from 1 to 8, and each chip with a pixel size 0.005 mm and 1024 pixels, including 16 dummy pixels, are organized into two rows and produce a 5772-pixel-wide image. The yellow arrow represents the flight direction.

2. RADIOMETRIC CALIBRATION

The radiometric calibration was conducted on the RSI within the satellite, in order to reduce non-uniformity and noise of images. The non-uniformity of ONGLAISAT images results variations in pixel responses and sensor positions.

2.1 Experimental Procedure

Figure 3 shows the experimental setup for radiometric calibration in the laboratory, in which ONGLAISAT is positioned in front of an integrating sphere to detect the uniform light.

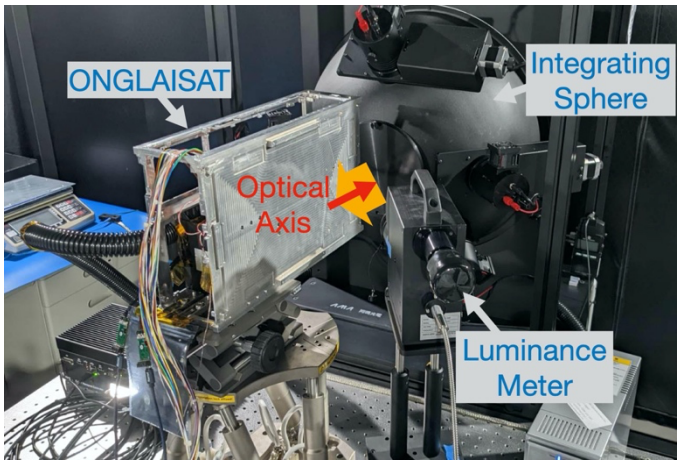

Figure 3. Experimental setup for radiometric calibration. ONGLAISAT is integrated in front of an integrating sphere. The telescope is aligned to the integrating sphere emitted light uniformly.

The digital numbers of the sensor are recorded at six brightness levels, using two TDI stages. Table 1 lists the radiance of incident light in the sensors' detectable wavelength range (450-900with nm) at six brightness levels. The radiance is measured by the luminance meter. For calibration purposes, dark current data was collected in two TDI stages. Each recorded data corresponds to one frame, consisting of 8192 pixels by 378 lines, with each line having a duration of 383 microseconds.

Brightness level	1	2	3	4	5	6
Radiance ($Wm^{-2}sr^{-1}$)	1.0124	1.5727	2.2093	2.9007	3.8906	5.0574

Table 1. The radiance of incident light at six brightness levels.

2.2 Calibration Data Analysis

The analysis of radiometric calibration data analysis aims to reduce the non-uniformly and noise of the sensor. The instrument response will be calibrated uniformly across all pixels at the same brightness levels using the record data taken from uniform light in Section 2.1. For this purpose, there are four processes proceeding in the following discussion. These processes, including the reduction of dark current data, calibration using typical method (Section 2.2.1), calibration using line regression method (Section 2.2.2), denoising using Fourier-wavelet transform, are referred to Process 1-4.

The DN values recorded when detecting the uniform light at six brightness levels are initially reduced by dark current data. This process is referred to Process 1. Figure 4 presents the image which passes Process 1, plotted based on the actual pixel positions. It's observed that these values are lower near the edges compared to the central area. The responses of the eight sensor chips are almost uniform before the RSI integration. Therefore, this variation is suggested to come from the RSI. The RSI, especially on two sides, partially blocks incoming light. The pixels where light is extinguished too much should be excluded. We deselect 350 pixels in Chip 1 and 275 pixels in Chip 5 to exclude the bad regions.

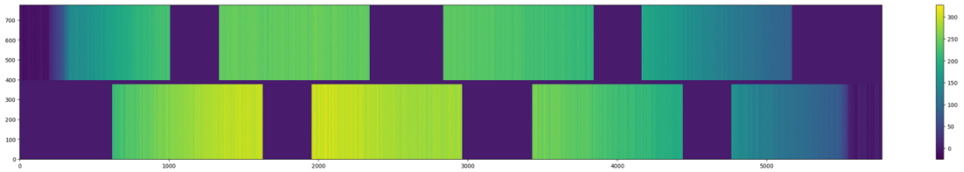

Figure 4. The recorded DN values when detecting a uniform light (input 1.5727 $Wm^{-2}sr^{-1}$ using TDI-8 stage). Each chip observes 378 lines. There are two rows of line sensor chips. The top chips are chips No. 1 to 4 from left to right. The bottom chips are No. 8 to 5 from left to right.

2.2.1 Typical Method

It is essential to define the priority pixels, which serves as the primary pixels when two pixels occupy the same position in the image. The overlapped pixels are selected if any issue arises with priority pixels.

To balance the effects of different chips, we select similar pixel numbers in each chip. Consequently, we chose 621, 621, 665, 665, 665, 666, 622, 622 pixels from Chip 1-8, respectively.

To reduce the gain effects pixel by pixel, we establish the benchmark images using an input light intensity setting at 1/3 of the sensors saturation level. The saturated DN value is 1024, and 1/3 saturation corresponding to 341.33. When the input light is 2.9007 $Wm^{-2}sr^{-1}$, the average recorded DN value is approximately 350, which closely matches the intensity at 1/3 saturation. Consequently, the benchmark is established the images when the input=2.9007 $Wm^{-2}sr^{-1}$.

The response of the i-th pixel in the RSI is defined by the following equation.

$$\mathrm{R(i)} = \frac{DN(i)}{\overline{DN}} \tag{1}$$

$DN(i)$ and $\overline{DN}$ are the DN value of the i-th pixel and the average DN value of all pixels, respectively. Figure 5 shows the responses using the benchmark (input=2.9007 $Wm^{-2}sr^{-1}$) using two TDI stages.

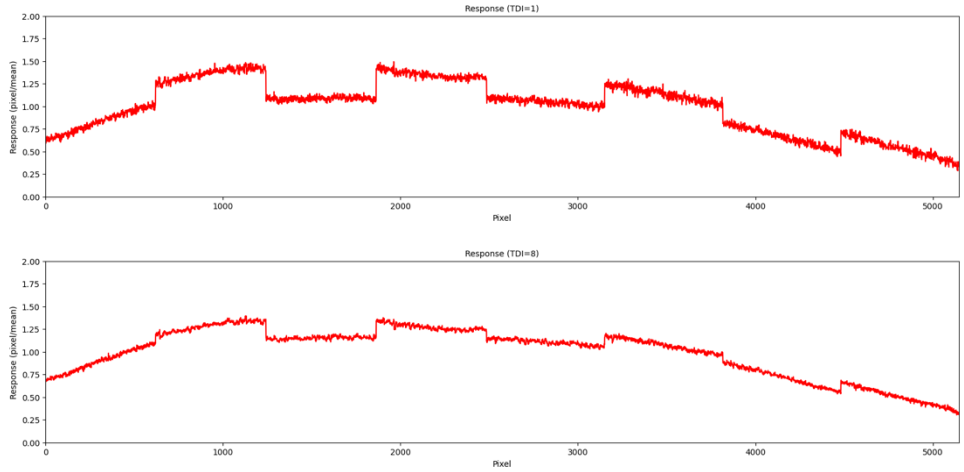

Figure 5. Responses (pixel/mean) of all pixels of benchmark (input=2.9007 $Wm^{-2}sr^{-1}$) using TDI=1 (top) and TDI=8 (bottom) stages.

Figure 6 shows DN values passing Process 1 are divided by these responses to radiometric calibrated values. This calibration process is referred to the typical method and Process 2. The errors using both TDI-1/8 stages are about 30/10. It is excessively noisy for future image processing. Therefore, we have explored another method instead of this one.

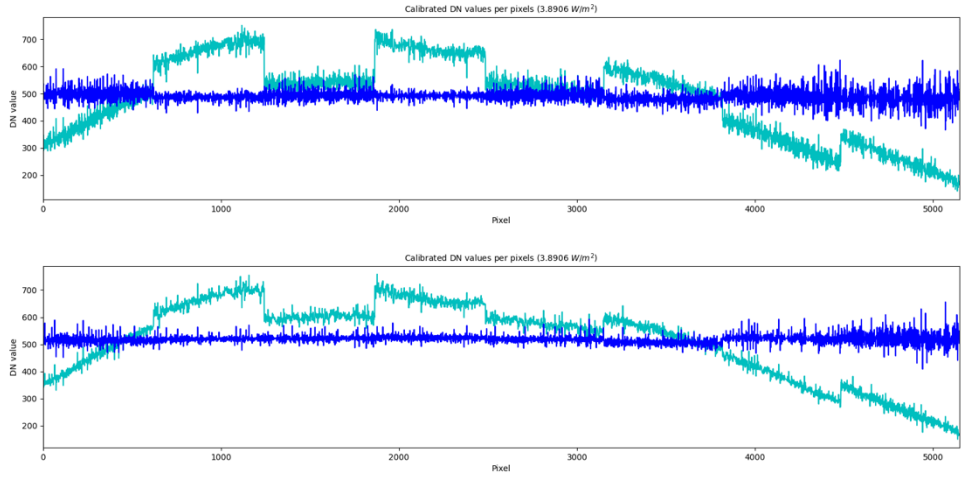

Figure 6. The comparison between DN values passing Process 1 (light blue) and calibrated (blue) DN values when input=3.8906 $Wm^{-2}sr^{-1}$ divided by the responses of benchmark (input=2.9007 $Wm^{-2}sr^{-1}$) using TDI=1 (top) and TDI=8 (bottom) stages.

2.2.2 Linear Regression Method

Based on the previous experiments, the linearity between input and output of the sensors is good. Due to this performance, we consider the response pixel by pixel by using a linear fitting between the input radiance and output DN values.

The 1/3 saturation situation (input=2.9007 $Wm^{-2}sr^{-1}$) is still set as the benchmark. For each pixel, we fit DN values with a linear equation. This line pass through the benchmark point (x_0, y_0)=(2.9007, DN(2.9007)) with a slope *m* where radiance is on the x-axis, and recorded DN values is on the y-axis.

$$y = \mathrm{m}(\mathrm{x} - x_0) + y_0 \tag{2}$$

Figure 7 shows the fitted lines using two TDI stages in one pixel.

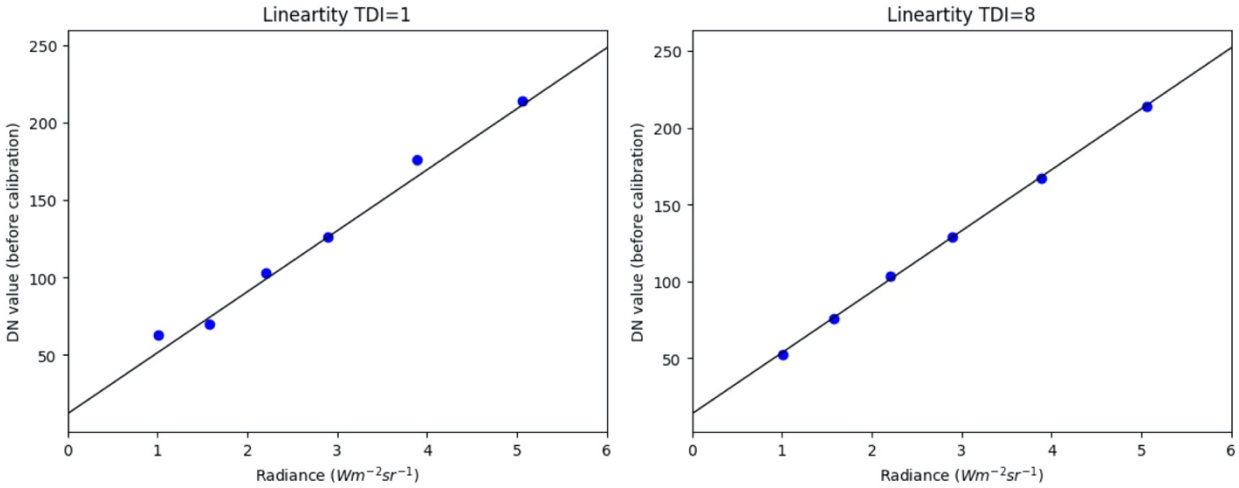

Figure 7. An examples for one of pixels. Fitted lines which pass through the benchmark point using TDI=1 (left) and TDI=8 (right) stages.

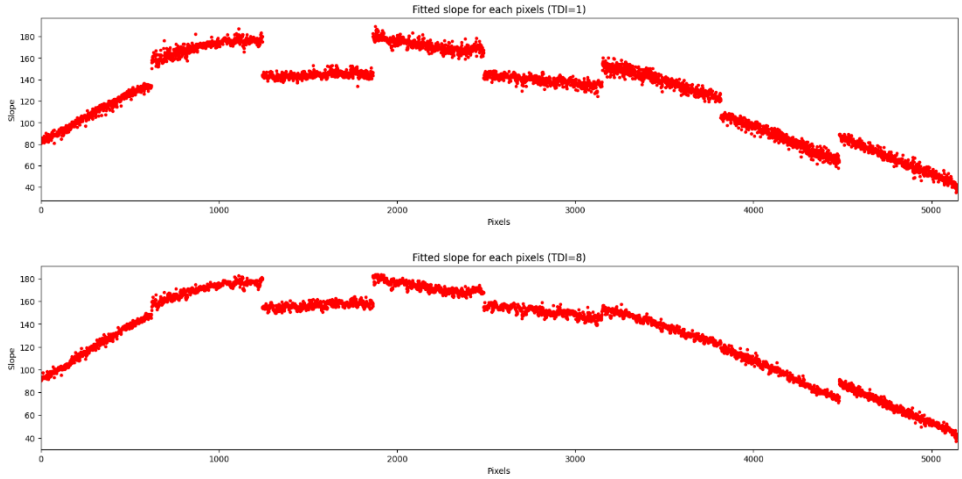

Figure 8. The slopes in all pixels using TDI=1 (top) and TDI=8 (bottom) stages.

Figure 8 shows the fitting slopes for all pixels. Using these slopes, the recorded DN values are calibrated to radiance by Equation 2. These radiance values are converted new DN values by Equation 2 which slope is the average of all slopes. Figure 9 shows the calibrated results using two different methods. It's evident that noise levels are significantly lower when employing the linear regression method using both TDI stages. Using TDI-8 stage, the steps caused by the chip effect differences are reduced more using the linear regression method. As a result, the linear regression method is chosen for the further analysis, and referred to Process 3. Nevertheless, there are still noticeable steps present, and the further denoising procedure are planned.

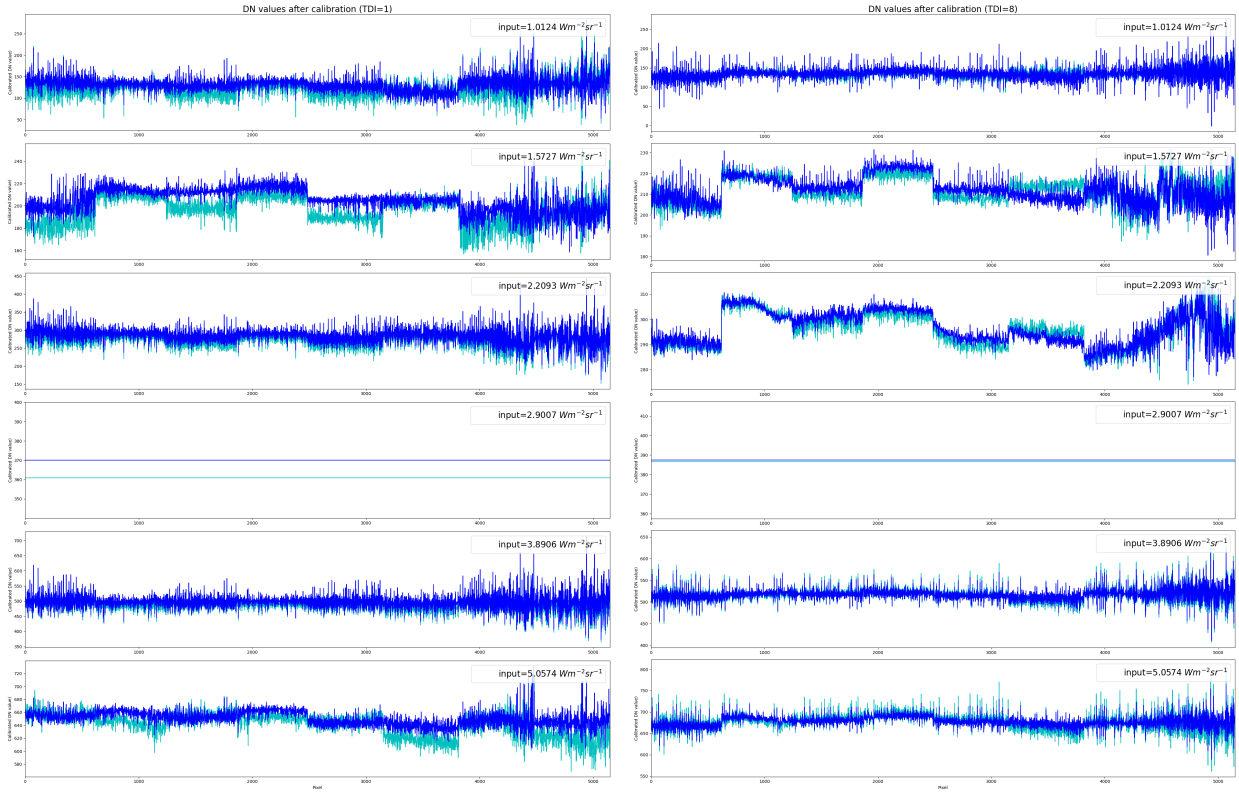

Figure 9. The calibrated results using TDI=1(left)/8(right) stages employing the typical (light blue) and line regression (blue) methods.

2.2.3 Filtering Methods for Denoising

The general denoising methods are Fourier transform and wavelet transform. The discrete Fourier transform (DFT) and the inverse discrete Fourier transform (IDFT) are employed for the 2D image denoising.

To reduce noise in each chip, all chip images are converted to power spectra using Fast Fourier Transform. Figure 10 shows an example which includes the image passing Process 1 and its 2D power spectra. In the power spectra, there is no dominant frequency along the y-axis.

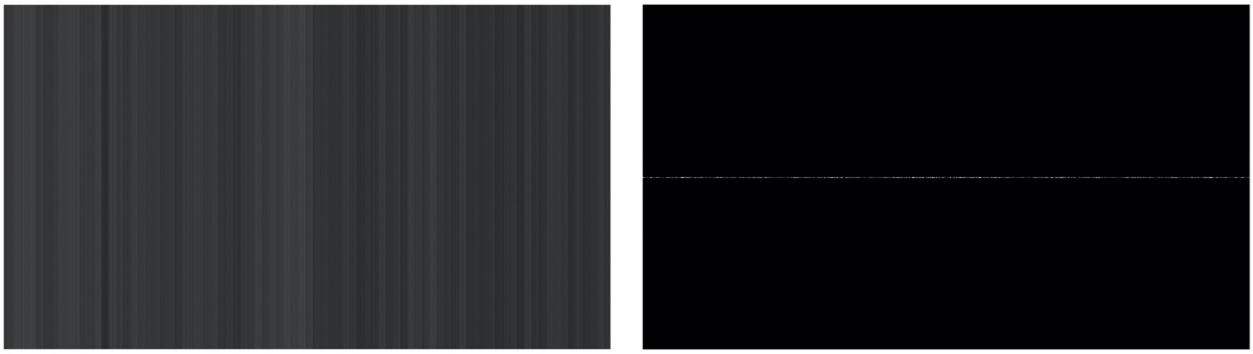

Figure 10. A chip image (left) and its average power spectra (right).

Figure 11 shows the power spectra in v=0. There are six dominant frequencies presenting in all chips. These frequencies are removed from all chip images before the inverse Fourier transform is applied.

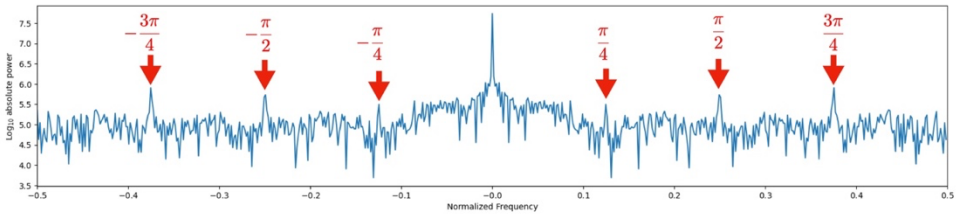

Figure 11. Log_{10} absolute power spectra when v=0. Six dominant frequencies are -π/4, π/4, where N=1,2,3.

The noise in all single chips has been reduced through Fourier transform. However, when combining eight Fourier-filtered chip images, it still introduces gain steps between chips. Additionally, we intend to flatten these filtered images using wavelet transform.

The wavelet analysis procedure involves adopting a wavelet prototype function, called an analyzing wavelet or mother wavelet. The combined original images are decomposed into a high and a low-frequency versions. Subsequently, these two versions are further decomposed into four components: high-high, high-low, low-high, and low-low.

This decomposition process is repeated until a certain frequency is identified, at which a pattern is similar to the gain step performance. Once this frequency is identified, it is removed, resulting in the partial flattening of the combined images. The process using Fourier-wavelet transform is referred to Process 4.

Figure 12 shows the results in all pixels passing Process 1, 3 (Section 2.2.2) with the final results passing Process 1, 3, 4. The figures noticeably appear flattened after the Fourier-wavelet transform.

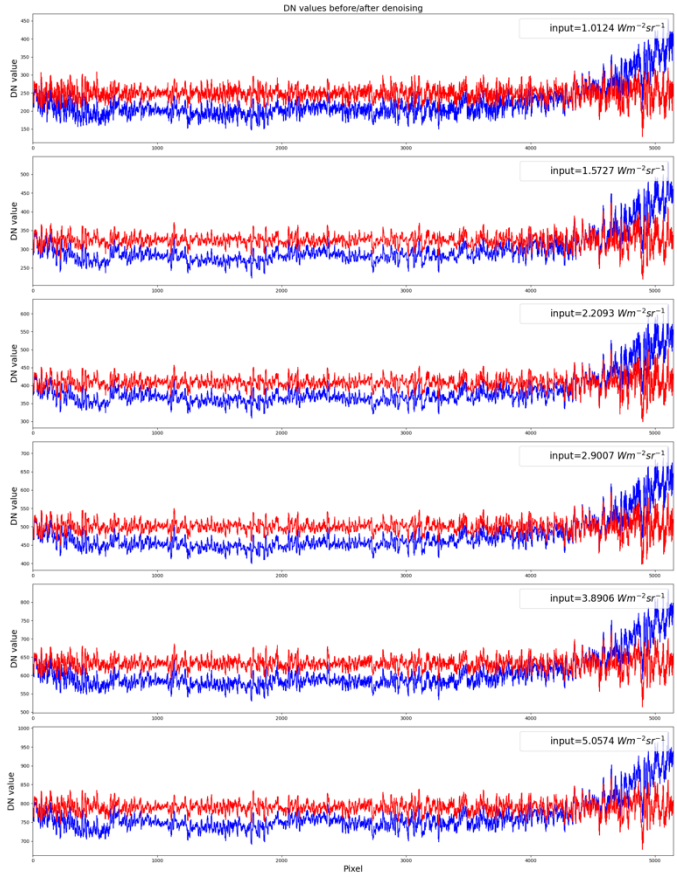

Figure 12 Time-averaged values in 6 brightness levels from the image passing Process 1, 3 (blue) and final results (red) passing Process 1, 3, 4.

Figure 13a compares the data passing Process 1 (Section 2.2.2) with the final results passing Process 1, 3, 4. The final results have undergone dark correction, radiometric calibration using the line regression method, and denoising using Fourier-wavelet transform. To make the results more comprehensible, Figure 13b displays these outcomes, which represent the averaged values over one frame time interval (378 lines) for each pixel. The images show that the non-uniformly and noise are both reduced by the previous calibration and denoising processes.

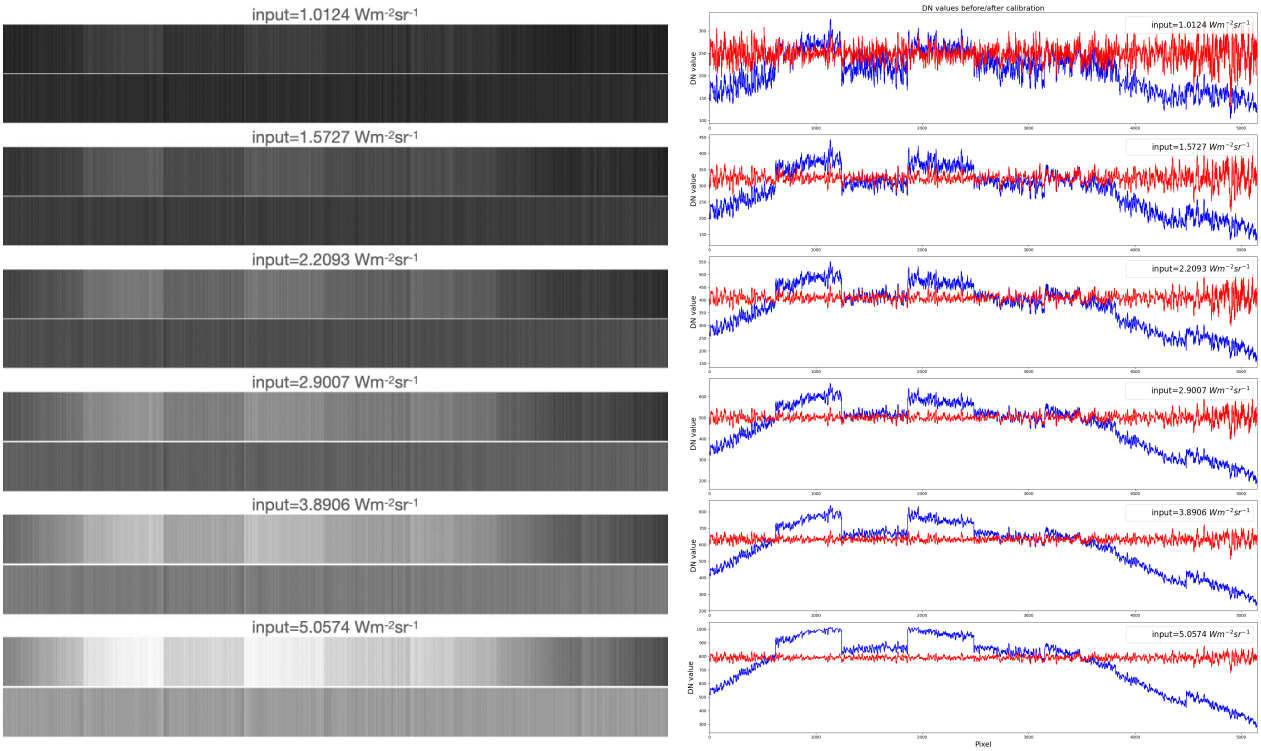

Figure 13a. (left) Six images passing Process 1 (top) and their final images (bottom) passing Process 1, 3, 4.
Figure 13b. (right) Time-averaged values from the image passing Process 1 (blue) and final results (red) passing Process 1, 3, 4.

2.3 Conclusion of Radiometric Calibration

The radiometric calibration work prior to launch is complete. The fitting slopes of each pixels and the Fourier-wavelet transform process will be used in the further ONGLAISAT image processing in orbit.

3. THE SENSOR ARRANGEMENT VERIFICATION

ONGLAISAT consists of the four front sensor chips and the four back sensor chips. Previous experiments have determined the corresponding positions of the front and back pixels. However, the distances between the two sensor rows are not verified. To combine the images pixel by pixel, it is necessary to determine the distance between a front-back pair chips in all seven overlapping regions.

3.1 Experimental Procedure

Figure 14 shows the experimental setup in the laboratory, collimator positioned in front of ONGLAISAT. The light emitted from the collimator passes through a double-slit target, producing two parallel line sources. This emission aligns on optical axis of the RSI.

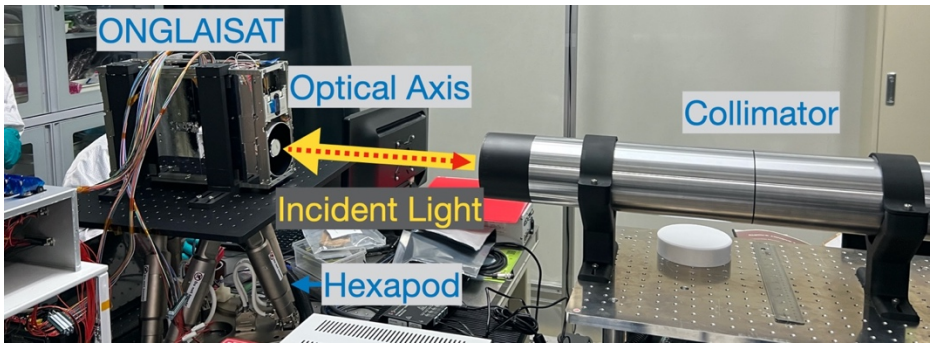

Figure 14. The laboratory setup for the sensor arrangement experiment. The collimator is positioned in front of ONGLAISAT which is mounted on the hexapod.

ONGLAISAT is mounted on a hexapod which can move in three axes. Figure 15 shows the three rotation directions are defined as U, V, W along x, y, x-axis.

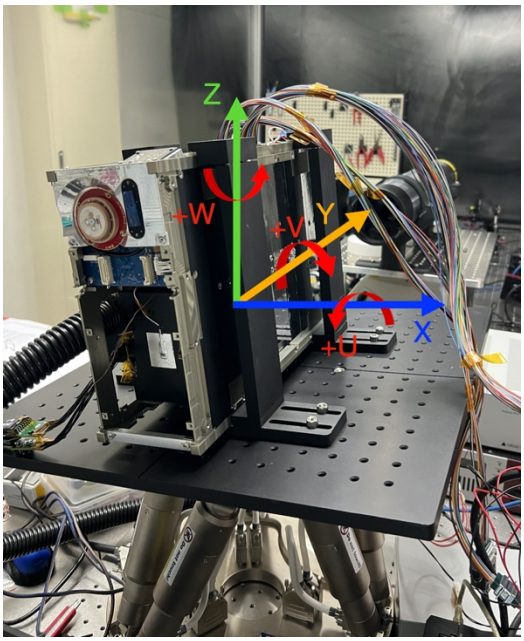

Figure 15. Rotation directions of the hexapod, +U, +V, +W along x, y, z-axis.

The method for determining the sensor arrangements involves detecting the double-slit line source at various incident angles. The geometric relationship of sensor chips can then be derived from these recorded components.

The double-slit line source is positioned to be parallel to the z-axis, while the sensor chips are aligned parallel to the x-axis. In each overlapping region, the data is recorded at different rotation angles. Figure 16 displays these three criteria. One criterion is that the sensors are perpendicular to the line source. The others involve the sensors rotating clockwise and counterclockwise in the +V/-V direction.

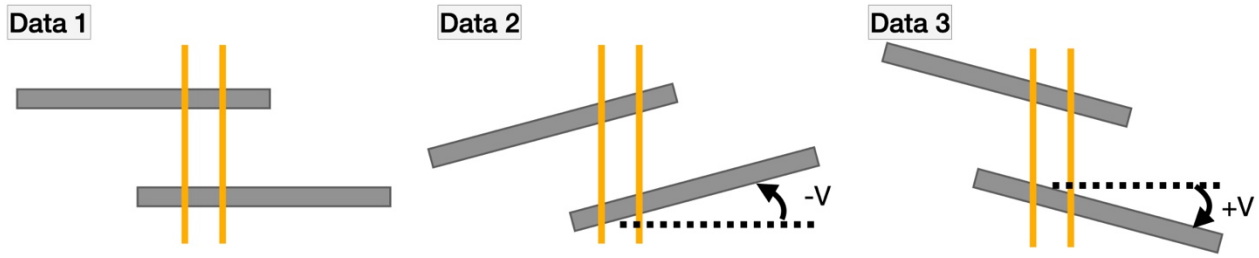

Figure 16. Three criteria at different incident angles through rotating RSI. Gray blocks are the sensor chips and yellow lines are the line source. Data 1: The source is vertical to sensors. Data 2: RSI moves in the -V direction. Data 3: RSI moves in the +V direction.

To determine the seven distances in all overlapping regions, the RSI is moved in the W-direction until the line source is positioned inside the first overlapping region, and then the source positions and the V angle are recorded. Subsequently, the RSI is moved in the -V/+V direction and these parameters are recorded once again. This process is repeated for each of seven overlapping regions.

3.2 Data Analysis

The geometric relationship can be calculated using single data pair. Figure 17 shows three data pairs in one overlapping region. The rotation angles θ and the distances in back(l)/front(L) chips between two data sets are recorded. Assuming the two chips parallel, the distances $d_{1,2}$, $d_{1,3}$, and $d_{2,3}$ can be obtained from each data pair.

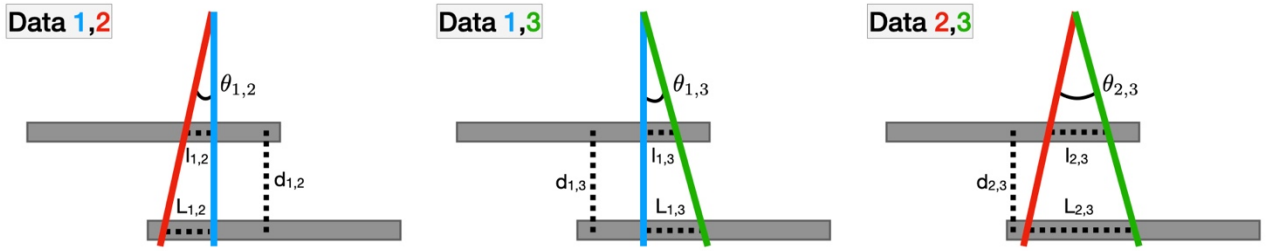

Figure 17. The geometric relationship in one of the overlapping regions. Three data pairs are defined by three data sets. The red, blue, green lines represent the line sources in Data 1, 2, 3.

The distances in the seven overlapping regions are calculated and shown in Table 2.

Distance between 2 overlapping chips (pixel)							
	Chip No.						
Data	4, 5	4, 6	3, 6	3, 7	2, 7	1, 7	1, 8
1, 2	112.26	102.27	126.22	284.19	145.34	66.22	167.54
1, 3	167.43	170.14	135.32	212.63	188.83	189.35	108.48
2, 3	140.07	136.11	130.80	226.92	164.14	124.51	138.15

Table 2. Calculated distances in 7 overlapping regions.

The distances look tens pixel difference in single overlapping region calculated by three data pairs. The value variation is from 10 to 60 except for the Chip 1, 7 region. The distances of the Chip 3, 7 region are much larger than the others.

This issue occurs because the positions of line sources are in pixel units. The calculated differences d would be 10-30 pixels if l or L has 1 pixel difference.

3.3 Conclusions of The Sensor Arrangement

The result of the sensor arrangement experiment defines the distances between the front-back sensors. The range is from 66 to 284 pixels. This experiment provides a range for searching in the further image combination in orbit.

4. CONCLUSIONS

In this article, the radiometric calibration and primary denoise of the 6U CubeSat ONGLAISAT are verified. The calibration process is going to be used for the further image processing in orbit. The distances between two line sensors are defined in a range (66-284 pixels). This will be the search range for the further image combination.

Acknowledgements

Thanks to all the project members for their support on the ONGLAISAT.

References

Chen-Yu Chan et al. 2022. Mission introduction of ONGLAISAT (ONboard Globe-Looking And Imaging Satellite). *10th Nano-Satellite Symposium (NSAT)*